Journal of Magnetic Resonance 303 (2019) 128–137

Contents lists available at ScienceDirect

Journal of Magnetic Resonance

journal homepage: www.elsevier.com/locate/jmr

Magnetohydrodynamic flow imaging of ionic solutions using electrical current injection and MR phase measurements

Hasan H. Eroğlu [a,*], Mehdi Sadighi [b], B. Murat Eyüboğlu [b]

[a] *Department of Electrical and Electronics Engineering, Bartın University, Bartın, Turkey*
[b] *Department of Electrical and Electronics Engineering, Middle East Technical University, Ankara, Turkey*

ARTICLE INFO

Article history:
Received 21 December 2018
Revised 16 April 2019
Accepted 23 April 2019
Available online 25 April 2019

Keywords:
Magnetohydrodynamics
Multiphysics model
Gradient echo
Bipolar flow encoding gradients
MR phase imaging

ABSTRACT

In this study, a method is proposed to image magnetohydrodynamic (MHD) flow of ionic solutions, which is caused by externally injected electrical current to an imaging media, during MRI scans. A multi-physics (MP) model is created by using the electrical current, laminar flow, and MR equations. The conventional spoiled gradient echo MRI pulse sequence with bipolar flow encoding gradients is utilized to encode the MHD flow. Using the MP model and the MRI pulse sequence, relationship between the MHD flow related phase in the acquired MR signal, the injection current, and the MRI pulse sequence parameters is stated. Numerical simulations and physical experiments are performed to validate the proposed method. The simulation and experimental results are in agreement and show that the MHD flow related MR phase depends on the amplitude and duration of the flow encoding gradient and the injected current. This method may be used to evaluate the MHD flow of conductive liquid media during MRI scans with simultaneous electrical current injections. The MHD flow related MR phase is 1.5 radian for an injected current of 1 mA amplitude, 30 ms duration and a flow encoding gradient amplitude of 24 mT/m. This large MR phase range exhibits potential use of this method for clinical applications such as investigation of highly conductive cerebrospinal fluid (CSF) during clinical use of electrical current based neuromodulation in MRI. However, very high and time varying velocities of typical CSF flow compared to the MHD flow velocities should also be considered.

© 2019 Elsevier Inc. All rights reserved.

1. Introduction

Magnetohydrodynamics (MHD) is the phenomena of interaction between magnetic fields and electrically conductive fluids. Principles of MHD can be identified by considering the generator and motor effects in conductive fluids. The generator effect is based on induction of electrical current in the fluid due to the interaction between the fluid flow and the magnetic flux density ($\boldsymbol{B}$). The motor effect is based on the fluid flow due to the current injected by an external source and $\boldsymbol{B}$ [1]. In MRI applications, conducting fluids interact with the static magnetic field ($\boldsymbol{B}_o$) of an MRI scanner. As a result, MHD effects are observed in the MR images of media comprising conductive fluids [2–5].

The MHD effects are well known in electrocardiogram (ECG) triggered MRI scans. In these applications, the interaction of blood flow with $\boldsymbol{B}_o$ induces current in the blood. The induced electrical current elevates the T-wave in the ECGs which is commonly interpreted as the MHD artifact [2,3,6–8]. It is reported that the MHD force does not affect the circulatory dynamics and the induced current is very low to stimulate the cardiac tissue [2,3]. However, the MHD artifact results improper R-wave detection in the ECG triggered MRI scans which require special algorithms to synchronize MR acquisition with the cardiac activity [6–8]. The interaction of electrical current and $\boldsymbol{B}_o$ in conductive fluids has been investigated in the literature [4,5,9–12]. Truong et al. proposed injecting current to an ionic solution in synchrony with a gradient-echo (GRE) pulse sequence [9]. They modeled the ionic motion considering the ionic velocity related drag force and the Lorentz force due to the ionic velocity and $\boldsymbol{B}_o$. They performed phantom experiments on a 4T MRI scanner and utilized oscillating gradients to encode the ionic motion. The acquired MR magnitude images exhibited signal loss related to the injected current and the encoding gradients [9].

Wijesinghe and Roth stated that the ionic mobility values used in [9] were unrealistic and the actual Lorentz force created by the ionic velocity and $\boldsymbol{B}_o$ was negligible [10]. They concluded that the MR signal loss in the experiments of [9] might be due to the MHD flow [10]. Pourtaheri et al. modeled the MHD flow in ionic

---

* Corresponding author.
E-mail addresses: heroglu@bartin.edu.tr (H.H. Eroğlu), mehdi.sadighi@metu.edu.tr (M. Sadighi), meyub@metu.edu.tr (B.M. Eyüboğlu).

https://doi.org/10.1016/j.jmr.2019.04.015
1090-7807/© 2019 Elsevier Inc. All rights reserved.

solutions during MRI experiments with current injection [4]. They concluded that the MR signal loss in the experiments of [9] was due to the MHD flow [4]. Balasubramanian et al. investigated the MHD flow in ionic solutions during echo planar imaging (EPI) scans including current injection [5]. They stated that the MR phase due to the MHD flow (Φ_{MHD}) was related to the injected current and the gradient fields of the EPI pulse sequence [5]. Imaging the MHD effects due to neural electric fields and $\boldsymbol{B}_o$ might provide useful information related to the neural activity [4,5]. Balasubramanian et al. stated that the MHD effects might change the cerebrospinal fluid (CSF) flow which might create an alternative functional MRI contrast mechanism especially in the case of epilepsy [5]. Although the experimental results in [4,5] state the potential of clinical application, physiological noise and actual flow dynamics of human body may suppress the MR signal variations related to the MHD flow.

It is observed that the MHD flow effects in the MR images were either demonstrated as the magnitude image artifacts or time evolution of the phase images obtained for conventional EPI gradients not specially designed for flow encoding purposes [4,5,9]. In this study, our goal is to analyze the MHD flow in ionic solutions during MRI scans. By this way, it is aimed to evaluate the feasibility of MHD flow imaging. The MHD flow is modeled by using the conservation of electrical current and laminar flow equations with suitable boundary conditions. The spoiled GRE pulse sequence with bipolar flow encoding gradients is synchronized to the electrical current injected to a phantom filled with an ionic solution. Considering the MRI pulse sequence parameters, electrical current continuity and laminar flow equations, a numerical model is created to simulate Φ_{MHD}. Phantom experiments are performed in order to validate the method.

2. MHD flow of ionic solutions during MRI scans with current injection

2.1. Fundamental equations of the MHD flow

Current injection to a body filled with an ionic solution under quasi-static conditions and solenoidal current flow can be expressed as

$$\nabla \cdot \boldsymbol{J} = \nabla \cdot (-\sigma \nabla V) = 0, \tag{1}$$

where $\boldsymbol{J}$ is the current density, σ is the electrical conductivity, and V is the scalar electrical potential. Eq. (1) can be solved with the following boundary conditions (BC)

$$\sigma \frac{\partial V(\boldsymbol{r})}{\partial \boldsymbol{n}} = \frac{I}{A} \ldots for\ \boldsymbol{r} \in e_+ \tag{2.1}$$

$$V(\boldsymbol{r}) = 0 \ldots for\ \boldsymbol{r} \in e_- \tag{2.2}$$

where $\boldsymbol{r}$ is the position, $\boldsymbol{n}$ is the surface normal, e_+ and e_- are the positive and negative electrodes, I is the amplitude of the injected current, and A is the area of the electrodes, respectively. The boundary value problem (BVP) shown in Eqs. (1) and (2) is solved for V, which is used to calculate the electric field, $E = -\nabla V$. During an MRI scan, the interaction of $\boldsymbol{J}$ and $\boldsymbol{B}_o$ creates an MHD force density ($\boldsymbol{F}$) throughout the solution as

$$\boldsymbol{F} = \boldsymbol{J} \times \boldsymbol{B}_o = \sigma(\boldsymbol{E} + \boldsymbol{v} \times \boldsymbol{B}_o) \times \boldsymbol{B}_o \tag{3}$$

according to the Lorentz Law, where $\boldsymbol{J} = \sigma(\boldsymbol{E} + \boldsymbol{v} \times \boldsymbol{B}_o)$ is the current density for a moving fluid with a velocity of $\boldsymbol{v}$. $\boldsymbol{F}$ can be expressed as summation of a rotating ($\boldsymbol{F}_r$) and a non-rotating force ($\boldsymbol{F}_{nr}$). In an enclosed system, $\boldsymbol{F}_{nr}$ is suppressed by the walls surrounding the fluid, whereas $\boldsymbol{F}_r$ results in the MHD flow [13]. Considering $\boldsymbol{E} \gg \boldsymbol{v} \times \boldsymbol{B}_o$ and using Ampere's Law, $\boldsymbol{F}$ can be expressed as

$$\boldsymbol{F} = \left[\frac{1}{\mu_o}(\nabla \times \boldsymbol{B}_J) + \sigma(\boldsymbol{v} \times \boldsymbol{B}_o)\boldsymbol{k}\right] \times \boldsymbol{B}_o\boldsymbol{k}, \tag{4}$$

where μ_o is magnetic permeability of free space, $\boldsymbol{B}_J$ is the magnetic flux density of $\boldsymbol{J}$, B_o is the intensity of $\boldsymbol{B}_o$, and $\boldsymbol{k}$ is the unit vector in the z-direction. Eq. (4) can be expanded as

$$\boldsymbol{F} = B_o\left[\left(\frac{1}{\mu_o}\frac{\partial B_{Jx}}{\partial z} - v_x B_o\right)\boldsymbol{i} + \left(\frac{1}{\mu_o}\frac{\partial B_{Jy}}{\partial z} - v_y B_o\right)\boldsymbol{j}\right] - \frac{B_o}{\mu_o}\nabla_t B_{Jz}, \tag{5}$$

where, B_{Jx}, B_{Jy}, B_{Jz} are the x, y, and z components of $\boldsymbol{B}_J$, v_x and v_y are the x and y components of v, $\nabla_t = \partial/\partial xi + \partial/\partial yj$ is the transverse gradient operator, $\boldsymbol{i}$ and $\boldsymbol{j}$ are the unit vectors in the x and y-directions, respectively. Using Eq. (5), $\boldsymbol{F}_r$ and $\boldsymbol{F}_{nr}$ can be expressed as

$$\boldsymbol{F}_r = \left[\left(\frac{1}{\mu_o}\frac{\partial B_{Jx}}{\partial z} - v_x B_o\right)\boldsymbol{i} + \left(\frac{1}{\mu_o}\frac{\partial B_{Jy}}{\partial z} - v_y B_o\right)\boldsymbol{j}\right] \tag{6.1}$$

$$\boldsymbol{F}_{nr} = -\frac{B_o}{\mu_o}\nabla_t B_{Jz} \tag{6.2}$$

since the curl of a gradient field is zero. $\boldsymbol{F}$ moves the fluid which can be modeled using the Navier-Stokes equation

$$\rho\left(\frac{\partial \boldsymbol{v}}{\partial t} + \boldsymbol{v} \cdot \nabla \boldsymbol{v}\right) = \nabla p + \mu \nabla^2 \boldsymbol{v} + \boldsymbol{F} \tag{7}$$

for incompressible fluids

$$\nabla \cdot \boldsymbol{v} = 0, \tag{8}$$

where ρ is the fluid density, p is the pressure field, and μ is the dynamic viscosity. In order to solve Eqs. (7) and (8) in an enclosed body, no-slip and open boundary conditions [11,12] are used as

$$\boldsymbol{v} = 0 \tag{9}$$

and

$$\boldsymbol{f}_o = 0, \tag{10}$$

where $\boldsymbol{f}_o$ is the normal stress on the boundaries. The BVP in Eqs. (7)–(10) is solved for $\boldsymbol{v}$, which is used to calculate the acceleration, $\boldsymbol{a} = \partial\boldsymbol{v}/\partial t$.

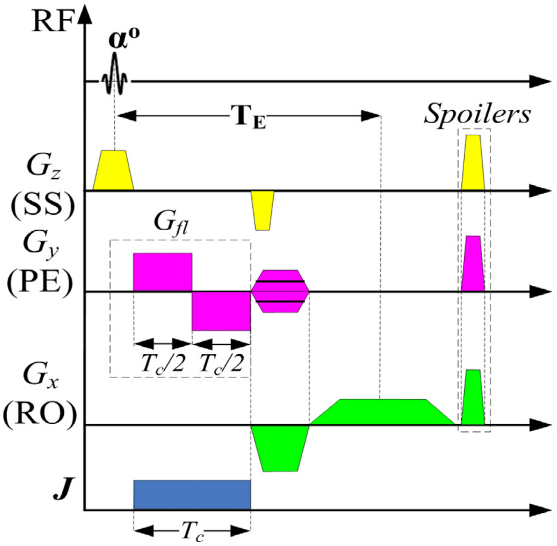

Fig. 1. A spoiled GRE pulse sequence with bipolar flow encoding gradients for encoding the MHD flow. RF stands for the RF pulse, G_z, G_y, and G_x are the slice selection (SS), phase encoding (PE) and read-out (RO) gradients, respectively.

2.2. Encoding the MHD flow

The MHD flow of an ionic solution can be encoded using the spoiled GRE pulse sequence with bipolar flow encoding gradients [14] and short repetition time (T_R) as shown in Fig. 1.

As shown in Fig. 1, $\boldsymbol{J}$ is injected to the ionic solution with a duration of T_c in synchrony with a bipolar flow encoding gradient (G_{fl}) in the y-direction after the α^o RF pulse. Therefore, the pulse sequence in Fig. 1 is capable of encoding the MHD flow in the y-direction. In order to encode the flow in the x-direction, G_{fl} can be applied to the read-out (G_x) gradient. After the $\boldsymbol{J}$ pulse and G_{fl}, the GRE signal is acquired. The MR phase image obtained as a result of this pulse sequence ($\Phi_{I,G_{fl}}$) can be expressed as

$$\Phi_{I,G_{fl}} = \Phi_o + \Phi_I + \Phi_{G_{fl}} + \Phi_{MHD-I,G_{fl}} + \Phi_{MHD-I,G_{Img}}, \tag{11}$$

where Φ_o is the systematic phase artifact of the MRI scanner including effects of the RF pulse and the imaging gradients (G_{Img}), Φ_I is the phase component due to current injection, $\Phi_{G_{fl}}$ is a non-zero phase distribution due to bipolar flow encoding gradients, $\Phi_{MHD-I,G_{fl}}$ and $\Phi_{MHD-I,G_{Img}}$ are the phase contributions of the MHD flow due to the injected current, G_{fl} and G_{Img}, respectively. $\Phi_{MHD-I,G_{fl}}$ can be extracted by removing $\Phi_o, \Phi_I, \Phi_{G_{fl}}$, and $\Phi_{MHD-I,G_{Img}}$ from the $\Phi_{I,G_{fl}}$ measurements. This can be achieved by using $\Phi_{I,G_{fl}}$ measurements with positive and negative I and G_{fl} polarities and taking the difference of the resultant $\Phi_{I,G_{fl}}$ distributions as

$$\Phi_{MHD-I,G_{fl}} = 0.25 \times [(\Phi_{I^+,G_{fl}^+} - \Phi_{I^-,G_{fl}^+}) - (\Phi_{I^+,G_{fl}^-} - \Phi_{I^-,G_{fl}^-})], \tag{12}$$

where $\Phi_{MHD-I,G_{fl}}$ is the measured Φ_{MHD} distribution. Φ_{MHD} can be expressed as

$$\Phi_{MHD} = \gamma \left[\frac{1}{T_c} \int_0^{T_c} G_y(\tau) y(\tau) d\tau \right] T_c, \tag{13}$$

where γ is the gyromagnetic ratio of hydrogen and y is the position. y can be expressed as

$$y(t) = y_0 + v_{oy} t + \frac{1}{2} a_y t^2, \tag{14}$$

where v_{oy} and a_y are y components of the constant velocity of the fluid (v_o) before the $\boldsymbol{J}$ pulse and the fluid acceleration during the $\boldsymbol{J}$ pulse, respectively. Considering the bipolar G_{fl} gradient in Fig. 1 and substituting Eq. (14) in Eq. (13) results

$$\Phi_{MHD} = -\gamma G_e \left(v_{oy} \frac{T_c^2}{4} + a_y \frac{T_c^3}{8} \right), \tag{15}$$

where G_e is the amplitude of G_{fl}. Φ_{MHD} changes as a function of time since v_{oy} and a_y are time varying distributions. Therefore, at each data acquisition period, k-space lines will be constructed with different Φ_{MHD} contributions. The k-space samples for the n^{th} data acquisition period can be expressed as

$$S[k_x, k_y, n] = \iint M(x, y) e^{-i2\pi(k_x x + k_y y)} e^{i\Phi_{MHD[x,y,n]}} dxdy, \tag{16}$$

where k_x and k_y are the spectral frequencies, and M is transverse magnetization of spins.

Velocity encodings at each data acquisition can be eliminated by utilizing bipolar $\boldsymbol{J}$ pulses with the pulse sequence in Fig. 1. For a bipolar $\boldsymbol{J}$ pulse with balanced lobes, v_y increases during the positive pulse and returns to zero at the end of the negative pulse. By this way, Φ_{MHD} expressed in Eq. (15) will be related to only a_y. However, removal of v_{oy} encoding will substantially reduce the magnitude of measured Φ_{MHD} distributions ($|\Phi_{MHD}|$). In this study, monopolar $\boldsymbol{J}$ pulses are preferred to bipolar $\boldsymbol{J}$ pulses in order to increase $|\Phi_{MHD}|$.

3. Simulation and experimental realization of MHD flow imaging

3.1. Numerical simulations

The experimental phantom is modeled in a Finite Element Method (FEM) solver, COMSOL Multiphysics 5.1 (COMSOL AB, Sweden) as shown in Fig. 2. The phantom has internal dimensions of 8 × 8 × 8 cm^3. Recessed electrodes of 2 × 2 cm^2 are located at 2 cm away from the center of the phantom walls. The phantom in the simulation model is filled with "Water, liquid" material from the library of COMSOL Multiphysics. σ value of the liquid material is changed as 0.75 S/m. The simulation model is composed of 74569 tetrahedral, 5070 triangular, and 440 edge elements, with the maximum and minimum element sizes of 5.19 mm and 0.98 mm, respectively. The BVP in Eqs. (1) and (2) is modeled using the *Electric Currents* interface of the solver. Electrical current (I) with a magnitude of 20 mA is applied to the phantom through the recessed electrodes oriented in the x-direction. The BVP in Eqs. (7)–(10) is modeled using the *Laminar Flow* interface of the solver. The open BC is applied for the top surface of the phantom and the no-slip BC is applied for the remaining surfaces. The laminar flow model is solved for a maximum step size of 1 ms.

As shown in Fig. 1, $\boldsymbol{J}$ is injected as a monopolar pulse during each T_R period. Therefore, $\boldsymbol{E}$ dependent component of $\boldsymbol{F}$ is adjusted as a periodic rectangular function for an electrical current duration of 10 ms and a period of 250 ms, which corresponds to T_R. Φ_{MHD} is reconstructed by considering Eqs. (15) and (16), and a rectilinear sampling procedure as shown in Fig. 3.

As shown in Fig. 3, v_o, a, k_y, and Φ_{MHD} at the n^{th} acquisition are updated at each phase encoding. The n^{th} k-space line is obtained by applying the Fourier transform to $\Phi_{MHD}[x, y, n]$. After the k-space sampling process, Φ_{MHD} is reconstructed by taking the inverse Fourier transform of the k-space signal, S. A uniform M distribution is taken in the simulated reconstructions. This is reasonable since the imaged medium is a uniform liquid and the MR phase effects that are not related to the MHD flow are removed by the phase difference operations shown in Eq. (12). Φ_{MHD} is reconstructed for different I, G_e, and T_c values.

3.2. Physical experiments

The experimental phantom shown in Fig. 2 is used in the experiments. Copper electrodes with dimensions of 2 × 2 cm^2 are located at the surfaces of the recessed structures. The phantom is filled with an ionic solution of 0.05 g $CuSO_4$ and 0.55 g NaCl in 100 ml distilled water. The conductivity of the solution is measured as 0.75 S/m (WTW ProfiLine Cond 3310, Xylem Analytics, Weilheim, Germany). The solution has a pH value of 5.26 (ZL20153 0145281.5, JuanJuan Elect. Tech. Co. Ltd, Guandong China). The MRI pulse sequence in Fig. 1 is implemented on a 3T clinical MRI scanner (MAGNETOM Trio, Siemens, Erlangen, Germany). The solution inside the phantom is renewed after each experiment. Experimental results are obtained for the transverse (xy) slice located at the center of the phantom. An external voltage controlled current source is used to inject current to the phantom through the recessed surface electrodes oriented in the x-direction [15]. The external current source is synchronized to the MRI pulse sequence by means of the optical trigger output of the scanner. Experimental parameters are listed in Table 1.

The experimental Φ_{MHD} measurements are compared with the Φ_{MHD} distributions reconstructed with the simulation data obtained for the same G_e, I, and T_c values.

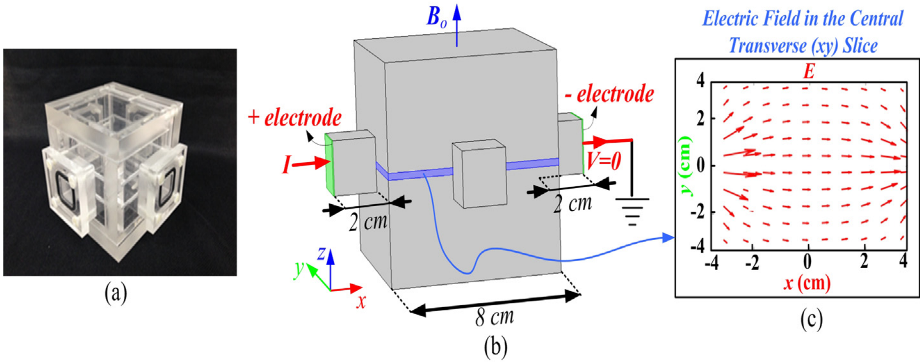

Fig. 2. The experimental phantom made of Plexiglas (a), geometrical structure of the phantom used in the numerical (FEM) simulations (b), and the electric field distribution in the central transverse slice (c).

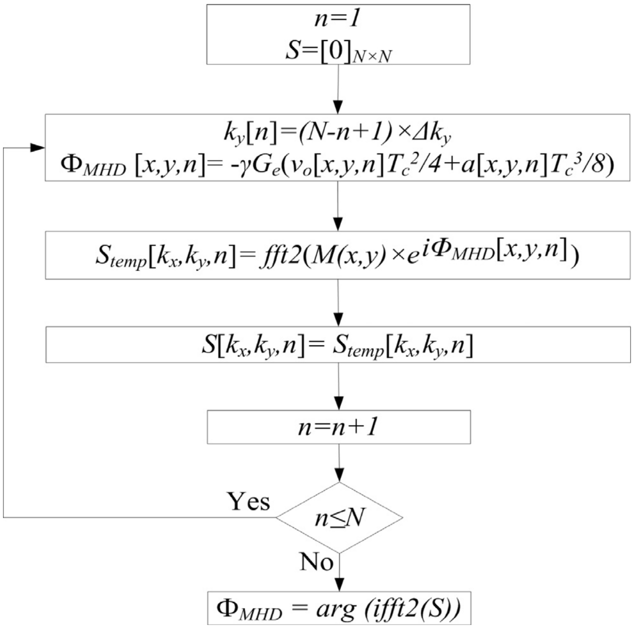

Fig. 3. The reconstruction procedure of Φ_{MHD}. N, arg(·), *fft*2(·), and *ifft*2(·) represent the number of phase encodings, the argument function, the two-dimensional fast Fourier transform (fft), and inverse fft, respectively.

4. Results

The simulated $\boldsymbol{E}$ distributions for $I = 20$ mA and the xy-slice at the center of the phantom are shown in Fig. 4.

As shown in Figs. 4(a, e, f), E_x is much greater than E_y since $\boldsymbol{J}$ is injected through the x-direction. As a result, $\boldsymbol{E}$ is also oriented in the x-direction as shown in Fig. 4(c). Magnitude of $\boldsymbol{E}$ ($|\boldsymbol{E}|$) changes as a function of distance to the electrodes.

The simulated magnitudes of $\boldsymbol{F}_r, \boldsymbol{F}_{nr}$, and $\boldsymbol{F}$ ($|\boldsymbol{F}_r|, |\boldsymbol{F}_{nr}|$, and $|\boldsymbol{F}|$) distributions are shown in Fig. 5. As shown in Fig. 5(a), $\boldsymbol{F}_r$ results fluid motion in −y–direction. On the other hand, direction of $\boldsymbol{F}_{nr}$ changes with respect to the center of the slice as shown in Fig. 5 (b). It is observed that $|\boldsymbol{F}_{nr}|$ values are very small along the central profiles of the slice. Therefore, the profiles shown in Fig. 5(d) are investigated instead of the central profiles in order to analyze the horizontal and vertical characteristics of $|\boldsymbol{F}_{nr}|$. On locations close to the electrodes, $|\boldsymbol{F}_{nr}|$ is comparable to $|\boldsymbol{F}_r|$ and $\boldsymbol{F}$ exhibits eddy behavior, as shown in Fig. 5(c). It is observed that $|\boldsymbol{F}_r|, |\boldsymbol{F}_{nr}|$, and $|\boldsymbol{F}|$ changes as a function of distance to the electrodes.

The simulated v distributions at the central xy-slice of the phantom for the 30th and 128th data acquisition periods are shown in Fig. 6. As shown in Fig. 6(a, b, d, e), both v_x and v_y depend on the distance to the electrodes and vary as a function of time. It is observed that v_x is much smaller than v_y especially in the regions away from the electrodes, whereas v_x and v_y become comparable in the regions near the electrodes. As shown in Fig. 6(c, f), v is oriented in -y-direction on locations away from the electrodes and eddy flow patterns are observed on locations close to the electrodes, which is consistent with the $\boldsymbol{F}$ distribution shown in Fig. 5(c). Time variation of v_y at different points in the central xy slice of the phantom are shown in Fig. 7. As shown in Fig. 7, v_y changes as a function of space and reaches the steady-state at different time instants for different locations.

The measured MR magnitude images are shown in Fig. 8. As shown in Fig. 8, the MHD flow does not create measurable changes in MR magnitude images. Therefore, further analysis is focused only on Φ_{MHD} images.

Images of the Φ_{MHD} measurements and the corresponding simulated images are shown in Figs. 9–11. As shown in Figs. 9–11, the experimental and simulated Φ_{MHD} measurements change as a function of I, G_e, and T_c which is consistent with Eq. (15). As shown in Fig. 9(a, b, d, e, g, h), $|\Phi_{MHD}|$ values increase as a function of I. However, the relationship between I and Φ_{MHD} is not linear. As shown in Fig. 9(a, d) and Fig. 9(c, f), Φ_{MHD} measurements scale with G_{ey} which

Table 1
Experimental parameters.

Exp.*	α (deg)	t_r* (μs)	T_R (ms)	Slice ST*/ (mm)	FOV*/ Sampling (cm^2/pix.)	I (mA)	G_{ex}* (mT/m)	G_{ey}* (mT/m)	T_c (ms)	T_E* (ms)
1	30	250	250	Central,xy/5	30 × 30/128 × 128	20	0	24	10	14.8
2						10				
3						20		12		
4						1		24	30	34.8
5						40	24	0	10	14.8
6							12			

* Exp., t_r, T_E, ST, FOV, G_{ex} and G_{ey} refer to experiment, rise time of G_{fl}, echo time, slice thickness, field of view, and amplitude of G_e in x and y directions, respectively.

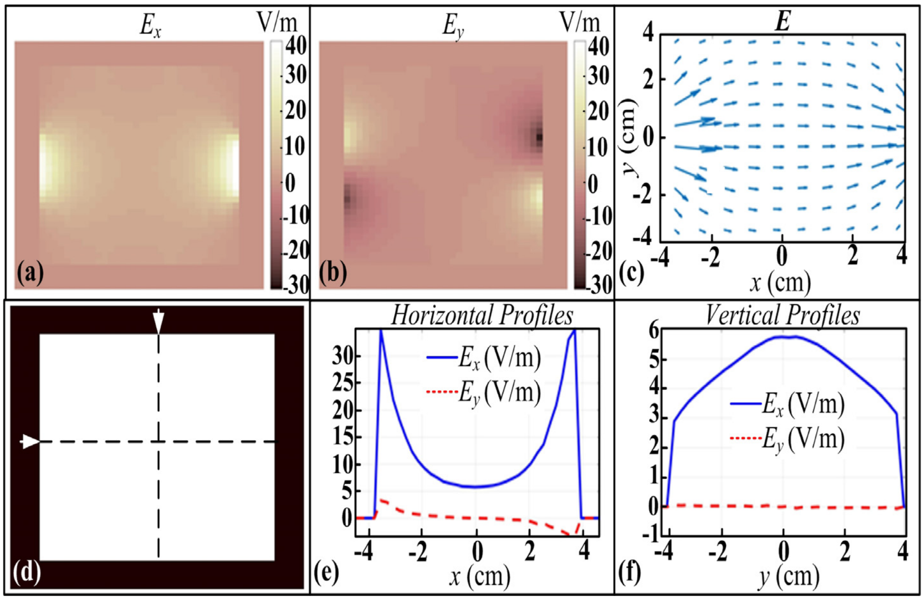

Fig. 4. The simulated $\boldsymbol{E}$ distributions (a-c) and profiles (e-f) at the central xy-slice of the phantom. E_x (a) and E_y (b), refer to the x and y components of $\boldsymbol{E}$, respectively. Horizontal and vertical profiles pass through the center of the slice as shown in (d).

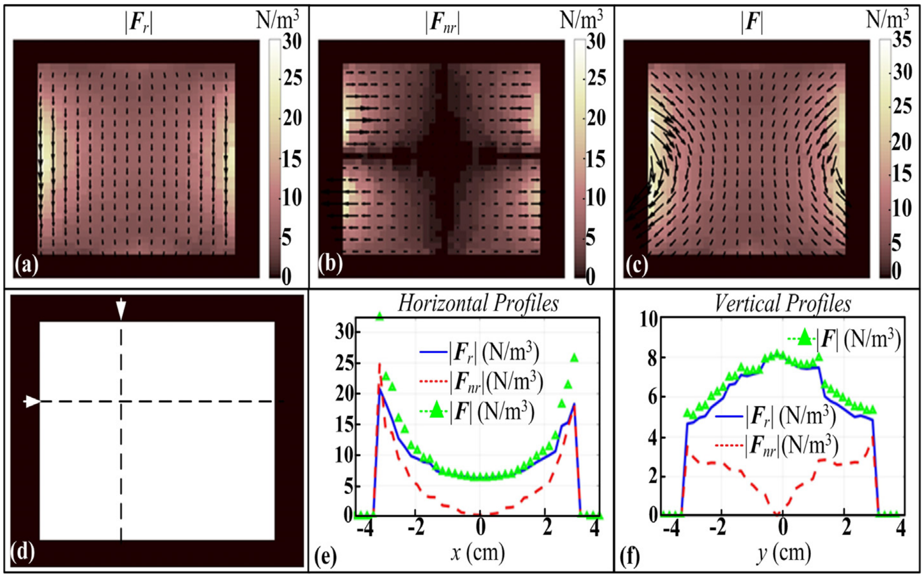

Fig. 5. The simulated $|\boldsymbol{F}_r|$, $|\boldsymbol{F}_{nr}|$, and $|\boldsymbol{F}|$ distributions (a-c) and the corresponding profiles (e-f) at the central xy-slice of the phantom as shown in (d).

seems to be more linear compared to the scaling obtained for the Φ_{MHD} images measured for different I. This is reasonable since Φ_{MHD} is directly related to G_{ey} as shown in Eq. (15), whereas the relationship between Φ_{MHD} and I can be constructed by using the multi-physics equations incorporating the electrical current and Navier Stokes equations as shown in Eqs. (1)–(15).

As shown in Fig. 10, the change in Φ_{MHD} with respect to T_c is very large since Φ_{MHD} is related to $v_{oy}T_c^2/4 + a_yT_c^3/8$ as shown in Eq. (15). Φ_{MHD} measurement range for $I = 1$ mA, $T_c = 30$ ms, $G_{ey} = 24$ mT/m is 1.5 radian, which is almost three times greater than the Φ_{MHD} measurement range for $I = 20$ mA, $T_c = 10$ ms, $G_{ey} = 24$ mT/m. It is seen that measurable Φ_{MHD} distributions can also be obtained for injected currents of small amplitudes and large durations. In experiments 1–4, it is seen that the experimental and simulated Φ_{MHD} measurements are similar. $|\Phi_{MHD}|$ increases in the regions close to the electrodes in which $|\boldsymbol{E}|$ is very high, whereas $|\Phi_{MHD}|$ decreases as a function of the distance to the electrodes, through which $|\boldsymbol{E}|$ becomes smaller. The simulation and experimental results show that the interaction of $\boldsymbol{J}$ with $\boldsymbol{B}_o$ induces the MHD flow in the -y-direction, which is encoded by G_{fl}. It is seen that the characteristics of the Φ_{MHD} measurements in Figs. 9 and 10 and the simulated v_y distributions in Fig. 6 are similar which exhibits the dominance of v_{oy} encoding in Φ_{MHD} measurements.

As shown in Fig. 11, the simulated and experimental Φ_{MHD} measurements in experiment 5–6 have qualitative similarity although considerable quantitative differences are observed between the simulated and experimental measurements. Quantitative differences between the simulated and experimental measurements are resulted from the low sensitivity of Φ_{MHD} measurements to v_x distributions inside the phantom. As shown in Fig. 4, the E_y values

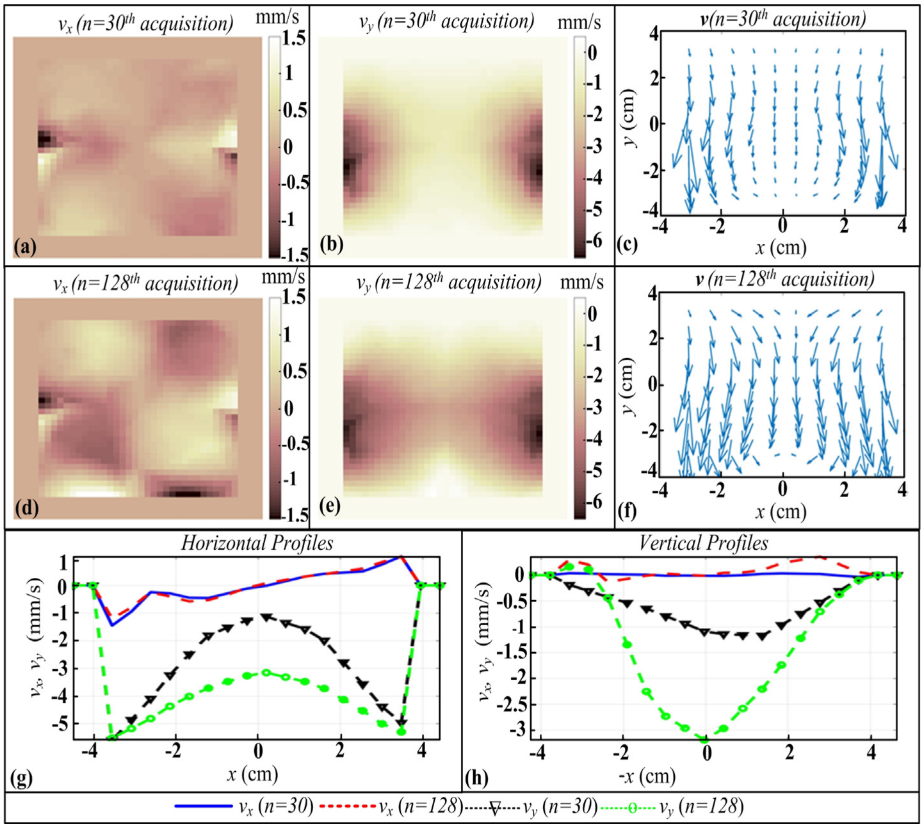

Fig. 6. The simulated v distributions (a-f) and profiles (g-h) at the central xy-slice of the phantom, for the $n = 30^{th}$ and $n = 128^{th}$ data acquisition periods. v_x (a, d) and v_y (b, e) refer to the x and y components of v, respectively. Locations of the horizontal and vertical profiles are shown in Fig. 4(d).

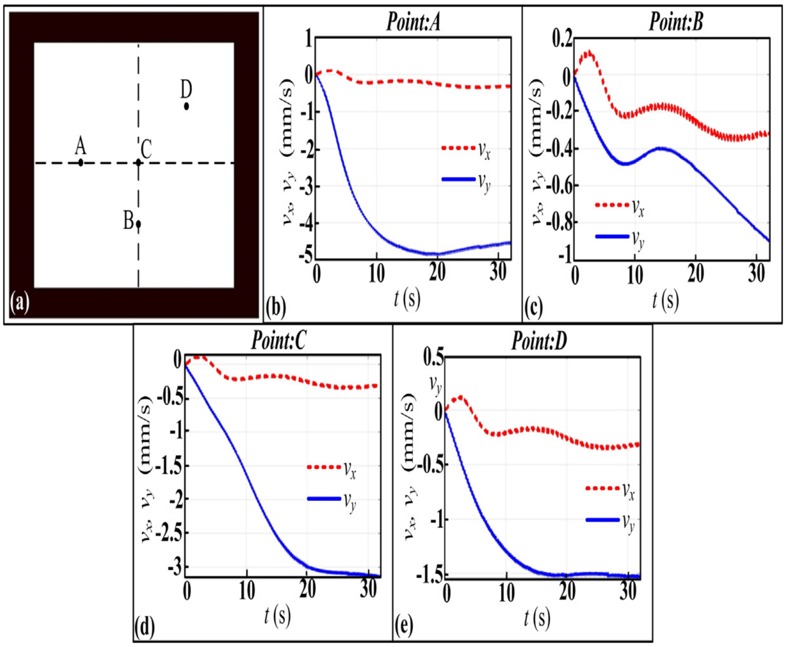

Fig. 7. Simulation results of $v_y(t)$ at different points (b-e) inside the selected slice. Locations of the selected points are shown in (a).

inside the phantom are very small since the current is injected through the electrodes oriented in the x-direction. As a result, v_x induced by the interaction of $\boldsymbol{B}_o$ and $\boldsymbol{J}$ are very weak, except at the locations that are close to the electrodes. It is seen that both the simulated and experimental Φ_{MHD} measurements show dependence on G_{ex}, which is consistent with Eq. (15). The characteristics

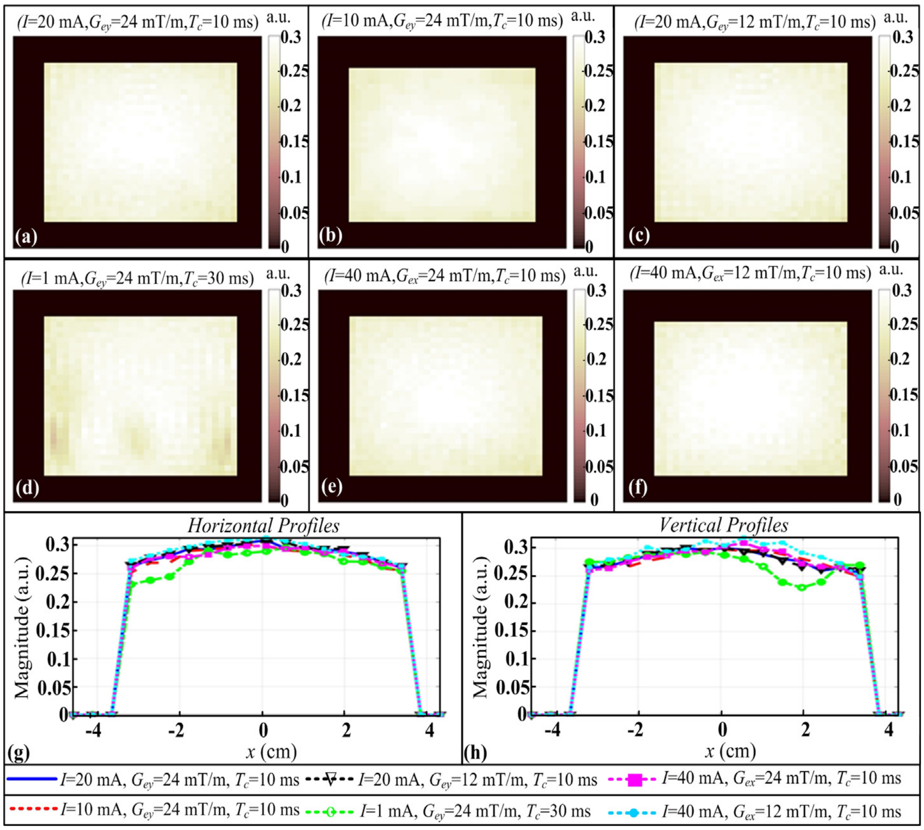

Fig. 8. The measured MR magnitude images of experiments 1 (a), 2 (b), 3 (c), 4 (d), 5 (e), 6 (f), and the corresponding horizontal and vertical profiles as shown in Fig. 4(d).

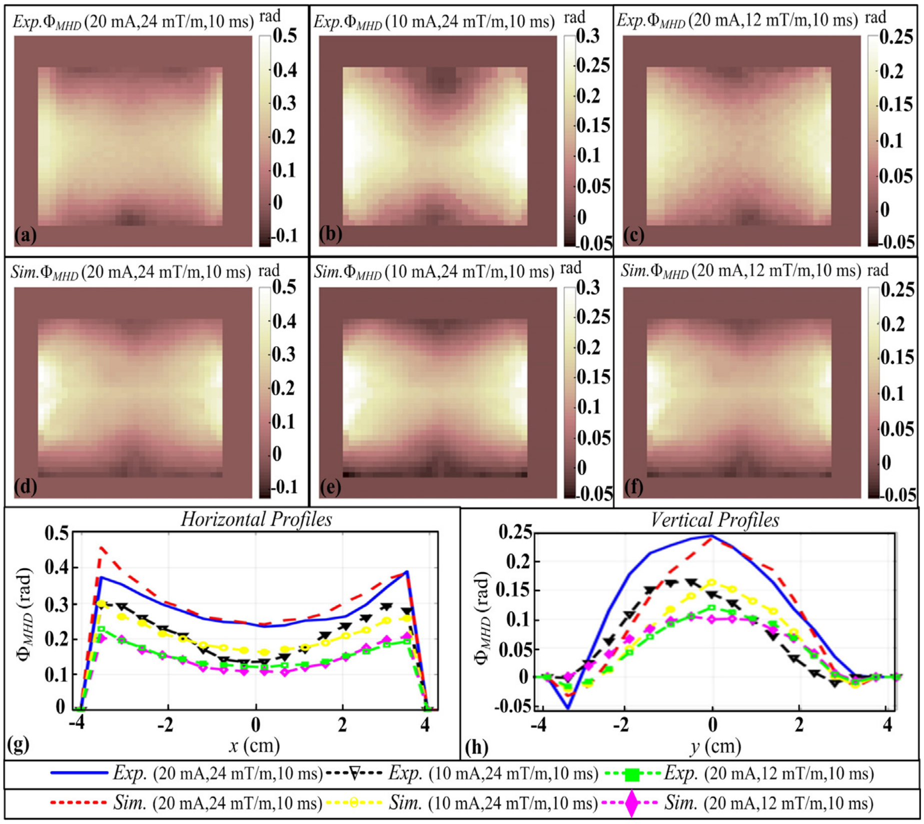

Fig. 9. The measured (exp.) and simulated (sim.) Φ_{MHD} images for experiments 1 (a, d), 2 (b, d), and 3 (c, f) with the horizontal (g) and vertical (h) profiles as shown in Fig. 4(d).

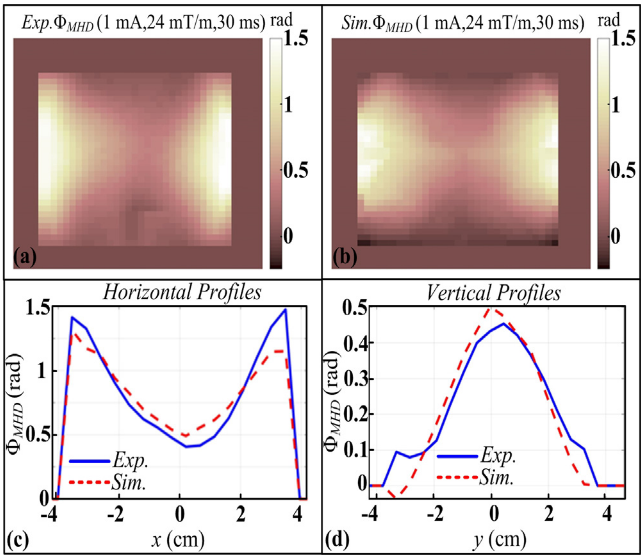

Fig. 10. The measured (a) and simulated (b) Φ_{MHD} images for experiment 4 with the horizontal (c) and vertical (d) profiles as shown in Fig. 4(d).

of the Φ_{MHD} measurements in Fig. 11 and the simulated v_x distributions in Fig. 5 are similar which exhibit the dominance of v_{ox} encoding in Φ_{MHD} measurements.

In order to evaluate the quantitative differences in the measured Φ_{MHD} images, root mean square (RMS) of the Φ_{MHD} distributions (Φ_{RMS}) are calculated as

$$\Phi_{RMS} = \sqrt{\frac{1}{N_i}\sum_{i=1}^{N_i}\Phi_{MHD}(i)^2}, \tag{17}$$

where i is the pixel index and N_i is the number of pixels in the selected slice. The calculated Φ_{RMS} values in experiments 1–6 are listed in Table 2. As shown in Table 2, the experimental and simulated Φ_{RMS} values obtained in experiments 1–6 are close to each other. As shown in experiments 1–2, the Φ_{RMS} values increase as a function of I. However, the relationship between Φ_{RMS} and I is not linear. On the other hand, the variation of Φ_{RMS} with respect to G_e is almost linear as shown in experiments 1, 3, 5, and 6. The largest Φ_{RMS} values are obtained in experiment 4 for $I = 1$ mA, $T_c = 30$ ms, $G_{ey} = 24$ mT/m. It is observed that the effect of T_c on Φ_{RMS} is much greater than the effect of I and G_e, which is consistent with Eq. (15).

Table 2
The Φ_{RMS} values in Experiments 1–6.

Exp.	Exp. Φ_{RMS} (rad)	Sim. Φ_{RMS} (rad)
1	0.211	0.215
2	0.173	0.176
3	0.116	0.108
4	0.683	0.613
5	0.033	0.027
6	0.066	0.053

5. Discussion

The experimental and simulated measurements show that imaging of the MHD flow is realized on a 3T clinical MRI scanner. The resultant Φ_{MHD} images are related to I, G_e, and T_c. Since this study aims to evaluate the feasibility of MHD flow imaging, in experiments 1, 2, 3, 5, and 6, I is injected at different levels as 10, 20, and 40 mA, which are very high for clinical applications. As shown in Eq. (15), I can be decreased by adjusting G_e and T_c appropriately. The increase in G_e is limited by the gradient system of MRI scanners. During the rise and fall time of G_{fl}, eddy current is also induced in the conductor media to be imaged. Therefore, in clinical applications, G_e and t_r should be considered together to prevent electrical stimulation of biological tissues due to the rapid gradient switching. As shown in Eq. (15), Φ_{MHD} is related to $v_{oy}T_c^2/4 + a_yT_c^3/8$. Therefore, increasing T_c is an efficient solution for reducing I as shown in experiment 4. However, the increase in T_c is limited by the effective transverse relaxation time (T2*) of the solution to be imaged. The measured MR signal and the corresponding measurement sensitivity of the method will be reduced due to very large increase in T_c.

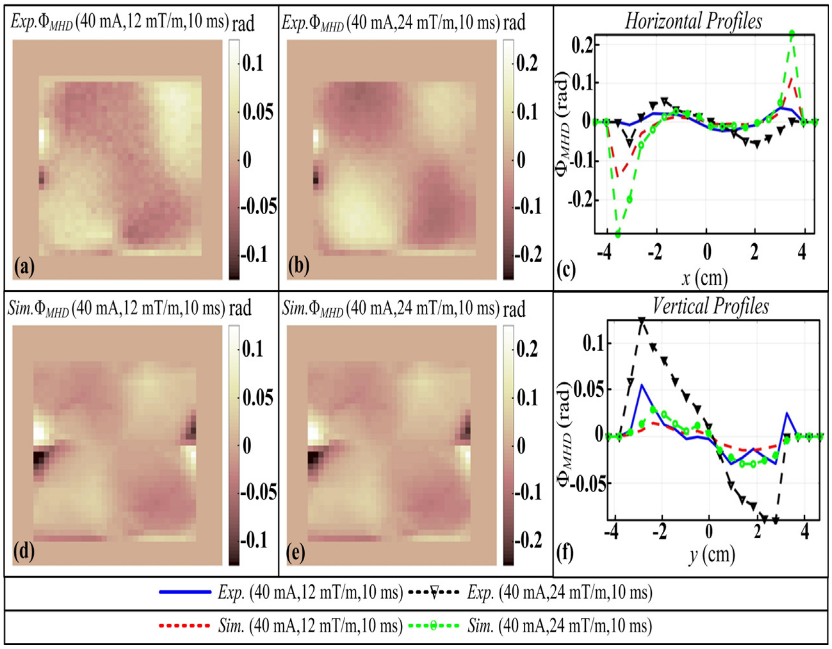

Fig. 11. The measured and simulated Φ_{MHD} images for experiment 5 (a, d) and 6 (b, e) with the horizontal (c) and vertical (f) profiles as shown in Fig. 4(d).

The remedy for increasing T_c may be the utilization of pulsed gradient spin-echo (PGSE) sequences used in diffusion and flow imaging applications [16–18]. In a PGSE sequence, flow encoding gradients are in either side of the refocusing RF pulse. Current should be injected between these flow-encoding gradients. It is recommended that the injected current should be zero during the refocusing RF pulse in order to prevent imaging artifacts due to the slice selection. Although the proposed single shot PGSE sequence can be viewed as an alternative solution for increasing the sensitivity of Φ_{MHD} measurements, its multi-echo implementation for shorter image acquisition time is not straightforward. Because, in a multi-echo PGSE sequence, the accumulated phase between the consecutive refocusing RF pulses is not equal due to the MHD flow which results the violation of the second Carr-Purcell-Meiboom-Gill (CPMG) condition [19,20]. On the other hand, the GRE pulse sequence in Fig. 1 can be easily converted to an EPI pulse sequence which will result in a shorter image acquisition time.

In addition to the potential multi-echo implementations of the MHD flow encoding sequences, the shape of flow encoding gradients should also be considered in order to generate Φ_{MHD} in a controllable way. The bipolar flow encoding gradients in Fig. 1 encode the constant velocity and acceleration terms together. As shown in Eq. (16) and Fig. 3, the MR phase contribution of the MHD flow is different at each data acquisition period, since v_o and a are time varying distributions. The change in Φ_{MHD} at each data acquisition interval can be reduced by removing the encoding of v_o. This can be achieved by using tripolar acceleration encoding gradients [21]. Utilization of tripolar acceleration encoding gradients may also reduce sensitivity to physiological noise over the presented pulse sequence with bipolar flow encoding gradients. However, the tripolar gradients will generate much smaller $|\Phi_{MHD}|$ values since sensitivity of Φ_{MHD} measurements to aT_c^3 encoding of the tripolar gradients is much smaller than sensitivity of Φ_{MHD} measurements to $v_oT_c^2 + aT_c^3$ encoding of the bipolar gradients. Injection of electrical current with very small amplitudes and large durations (in the order of minutes) may be used for creating a stable MHD flow which may also provide consistent velocity encodings at each T_R. If the injection current is not switched off during the pulse sequence, phase artifacts related to electric current may be created. On the other hand, if the injection current is switched off prior to the pulse sequence, the velocity distributions will deviate from the steady state as a function of both position and time which may result different velocity encoding at each T_R. Injection of monopolar electric current with very large duration (in the order of minutes) may also polarize the solution. It is more natural to apply the electric current with small durations instead of a single pulse with large duration.

Experimental results do not exhibit substantial changes in the MR magnitude images acquired for different I, G_e, and T_c, in contrast to [4,9]. Observed changes are only in Φ_{MHD}. As shown in Eq. (15), very high G_e values and injected current durations may result excessive Φ_{MHD} accumulation in the MR signal which may also degrade the MR signal quality. Utilization of copper electrodes may reduce signal to noise ratio (SNR) of experiments due to magnetoelectrolysis similar to the nuclear magnetic resonance (NMR) experiments in [22]. SNR can be improved by using carbon electrodes. Experimental results of the present study are also in line with [5] which also evaluates the MHD flow effects during EPI scans by inspecting the MR phase images. However, in order to perform the MHD flow experiments in a more controllable fashion, utilization of the flow encoding gradients are recommended instead of the gradients of conventional EPI pulse sequences as used in [5].

Effects of the MHD flow have also been studied in MR current density imaging (MRCDI) and MR electrical impedance tomography (MREIT) applications [11-13]. Scott et al. discussed that the MHD flow of solutions inside a phantom might produce a phase shift during an MRCDI scan. They expressed that the MHD flow induced phase shift disappeared when the phantom was filled with a gel or by using a pulse sequence with reduced motion sensitivity [13]. Minhas et al. investigated the MHD flow effects in MREIT experiments [11,12]. They used injected current non-linear encoding (ICNE) method in synchrony with a spin-echo (SE) MRI pulse sequence on an 18.8T MRI scanner [11]. It is known that the ICNE method extends the current injection duration to the RO intervals to increase Φ_I [23], which results encoding of the MHD flow by the RO gradients. In a more recent study, Minhas et al. extended [11] by considering the MREIT experiments with SE and GRE sequences [12]. They used phantoms composed of artificial sea water and agarose. In both [11,12], it was reported that the MHD flow of the ionic solution affected the MR phase measurements, whereas the MR phase measurements of the highly viscous agarose was free from the MHD effects. The results in [11,12] are in line with the present study. As shown in Eqs. (3)–(7), the MHD flow due to E_x and E_y (v_y and v_x) can be encoded by G_{ey} and G_{ex}, respectively. Therefore, the injection current direction should be parallel to the RO direction in order not to encode the MHD flow in MREIT experiments.

Both the literature [4,5] and the present study show that imaging of the MHD flow is only applicable in pure liquid media. Since porous media is more relevant to the biological tissues, it is difficult to find a clinical application for MHD flow imaging. However, in biological systems, porous and liquid media are in the neighborhood of each other. For example, the highly conductive CSF, which has an electrical conductivity value of 1.79 S/m in the body temperature, is close to excitable neural tissues [24]. Balasubramanian et al. expressed that the generation of large electrical fields near CSF during the epileptic seizures might induce an MHD flow which might also alter the usual CSF flow related to the cardiac cycle. It was stated that the imaging of MHD dependent changes in the CSF flow might provide direct information about the neural system [5]. Another potential application area of the MHD flow imaging is the investigation of CSF flow during the utilization of neuromodulation techniques, such as transcranial electrical stimulation (TES), transcranial magnetic stimulation (TMS), and deep brain stimulation (DBS). These neuromodulation techniques may create large electrical fields which may induce MHD dependent changes in the CSF flow. Experimental parameters of $I = 1$ mA, $T_c = 30$ ms, $G_{ey} = 24$ mT/m results a large Φ_{MHD} range of 1.5 radian which exhibits potential for the mentioned clinical applications. However, in clinical applications, the usual CSF flow velocities due to cardiac rhythm will also contribute to Φ images obtained as a result of the proposed pulse sequence. As reported in [25], the usual CSF velocities are in the order of cm/s, which are much greater than the reported MHD flow velocities in the order of mm/s. The reported CSF velocities are time-dependent considerably. Therefore, reconstruction of Φ_{MHD} distributions by using Eq. (12) may not effectively eliminate the effects of the usual CSF flow. In this study, pure liquid media is considered in order to investigate the feasibility of MHD flow imaging. However, in clinical applications, non-liquid inhomogeneities may exist in the imaged liquid medium. These inhomogeneities may attenuate the MR signal and deviate the MHD flow patterns. In order to evaluate the potential of the presented method in the mentioned clinical applications, non-uniform media should also be investigated.

6. Conclusion

In this study, imaging of the MHD flow is realized by using a conventional GRE pulse sequence with bipolar flow encoding gradient and injection current pulses. The measured Φ_{MHD} images are related with I, G_e, and T_c in consistent with the theory. The proposed method can be used to understand the MHD flow in conductive liquid media, during MRI scans including current injections. The proposed method may be used to evaluate the changes in the flow of liquid media located near excitable tissues, such as CSF. However, very high and time varying velocities of the usual CSF flow may suppress the phase changes due to the MHD flow.

Acknowledgement

MRI experiments were performed at UMRAM (National Magnetic Resonance Research Center), Bilkent University, Ankara, Turkey. The authors would like to thank the referees and the associate editor for their rigorous review, constructive comments, discussions, and recommendations which certainly improved quality of the manuscript.

References

[1] P.A. Davidson, An Introduction to Magnetohydrodynamics, Cambridge University Press, New York, 2001.
[2] T. Budinger, Emerging nuclear magnetic resonance technologies. health and safety, Annals of the, New York Acad. Sci. 649 (1) (1992) 1–18, https://doi.org/10.1111/j.1749-6632.1992.tb49592.x.
[3] D.J. Schaefer, J.D. Bourland, J.A. Nyenhuis, Review of patient safety in time-varying gradient fields, J. Magn. Reson. Imaging 12 (1) (2000) 20–29, https://doi.org/10.1002/1522-2586(200007)12:1<20::AID-JMRI3>3.0.CO;2-Y.
[4] N. Pourtaheri, T.-K. Truong, C.S. Henriquez, Electromagnetohydrodynamic modeling of Lorentz Effect Imaging, J. Magn. Reson. 236 (2013) 57–65, https://doi.org/10.1016/j.jmr.2013.08.011.
[5] M. Balasubramanian, R.V. Mulkern, W.M. Wells, P. Sundaram, D.B. Orbach, Magnetic resonance imaging of ionic currents in solution: the effect of magnetohydrodynamic flow, Magn. Reson. Med. 74 (4) (2015) 1145–1155, https://doi.org/10.1002/mrm.25445.
[6] J.M. Chia, S.E. Fischer, S.A. Wickline, C.H. Lorenz, Performance of QRS detection for cardiac magnetic resonance imaging with a novel vectorcardiographic triggering method, J. Magn. Reson. Imaging 12 (5) (2000) 678–688, https://doi.org/10.1002/1522-2586(200011)12:5<678::AID-JMRI4>3.0.CO;2-5.
[7] G.M. Nijm, S.S. Swiryn, A.C. Larson, A.V. Sahakian, Extraction of the magnetohydrodynamic blood flow potential from the surface electrocardiogram in magnetic resonance imaging, Med. Biol. Eng. Comput. 46 (7) (2008) 729–733, https://doi.org/10.1007/s11517-008-0307-1.
[8] T. Frauenrath, K. Fuchs, M.A. Dieringer, C. Özerdem, N. Patel, W. Renz, A. Greiser, T. Elgeti, T. Niendorf, Detailing the use of magnetohydrodynamic effects for synchronization of MRI with the cardiac cycle: a feasibility study, J. Magn. Reson. Imaging 36 (2) (2012) 364–372, https://doi.org/10.1002/jmri.23634.
[9] T.-K. Truong, A. Avram, A.W. Song, Lorentz Effect Imaging of ionic currents in solution, J. Magn. Reson. 191 (1) (2008) 93–99, https://doi.org/10.1016/j.jmr.2007.12.005.
[10] R.S. Wijesinghe, B.J. Roth, Lorentz Effect Imaging of ionic currents in solution using correct values for ion mobility, J. Magn. Reson. 204 (2) (2010) 225–227, https://doi.org/10.1016/j.jmr.2010.02.024.
[11] A.S. Minhas, M. Chaucan, R.J. Sadleir, Analysis of magnetohydrodynamic effects in current injection induced magnetic flux density images at very high magnetic fields, in: Proceedings of the 25th Annual Meeting of the International Society of Magnetic Resonance in Medicine, Honolulu, Hawai, 2017, p. 1005.
[12] A.S. Minhas, M. Chaucan, F. Fu, R.J. Sadleir, Evaluation of magnetohydrodynamic effects in magnetic resonance electrical impedance tomography at ultra high magnetic fields, Magn. Reson. Med. (2019), https://doi.org/10.1002/mrm.27534.
[13] G.C. Scott, M.L.G. Joy, R.L. Armstrong, R.M. Henkelman, Measurement of nonuniform current density by magnetic resonance, IEEE Trans. Med. Imaging 10 (3) (1991) 362–374, https://doi.org/10.1109/42.97586.
[14] M.A. Bernstein, K.F. King, X.J. Zhou, Flow-encoding gradients, in: Handbook of MRI Pulse Sequences, Elsevier Academic Press, New York, 2001, Ch. 9, pp. 281–291. https://doi.org/10.1016/B978-012092861-3/50014-5.
[15] H.H. Eroglu, B.M. Eyuboglu, C. Goksu, Design and implementation of a bipolar current source for MREIT applications, in: Proceedings of the IFMBE 13th Mediterranean Conference of Medical and Biological Engieering and Computing (MEDICON), Sevilla, Spain, 2013, pp. 161–164, https://doi.org/10.1007/978-3-319-00846-2_40.
[16] E.O. Stejskal, J.E. Tanner, Spin diffusion measurements: Spin-echoes in the presence of a time dependent field gradient, J. Chem. Phys. 42 (1) (1965) 288–292, https://doi.org/10.1063/1.1695690.
[17] D.J. Bryant, J.A. Payne, D.N. Firmin, D.B. Longmore, Measurement of flow with NMR imaging using a gradient pulse and phase difference technique, J. Comput. Assist. Tomogr. 8 (4) (1984) 588–593.
[18] L.F. Gladden, A.J. Sederman, Recent advances in flow MRI, J. Magn. Reson. 229 (2013) 2–11, https://doi.org/10.1016/j.jmr.2012.11.022.
[19] H.Y. Carr, E.M. Purcell, Effects of diffusion on free precession in nuclear magnetic resonance experiments, Phys. Rev. 94 (3) (1954) 630–638, https://doi.org/10.1103/PhysRev. 94.630.
[20] S. Meiboom, D. Gill, Modified spin-echo method for measuring nuclear relaxation times, Rev. Sci. Instrum. 29 (8) (1958) 688–691, https://doi.org/10.1063/1.1716296.
[21] J.-P. Tasu, O. Jolivet, E. Mousseaux, A. Delouche, B. Diebold, J. Bittoun, Acceleration mapping by fourier acceleration-encoding: in vitro study and initial results in the great thoracic vessels, Magn. Reson. Med. 38 (1) (1997) 110–116, https://doi.org/10.1002/mrm.1910380116.
[22] B.F. Gomes, L.M.S. Nunes, C.M.S. Lobo, L.F. Cabecca, L.A. Colnago, In situ study of the magnetoelectrolysis phenomenon during copper electrodeposition using time domain nmr relaxometry, Anal. Chem. 86 (19) (2014) 9391–9393, https://doi.org/10.1021/ac502361q.
[23] C. Park, B.I. Lee, O. Kwon, E.J. Woo, Measurement of induced magnetic flux density using injection current nonlinear encoding (ICNE) in MREIT, Physiol. Meas. 28 (2) (2007) 117–127, https://doi.org/10.1088/0967-3334/28/2/001.
[24] S.B. Baumann, D.R. Wozny, S.K. Kelly, F.M. Meno, The electrical conductivity of human cerebrospinal fluid at body temperature, IEEE Trans. Biomed. Eng. 44 (3) (1997) 220–223, https://doi.org/10.1109/10.554770.
[25] M.C. Henry-Feugeas, I. Idy-Peretti, B. Blanchet, D. Hassine, G. Zannoli, E. Schouman-Claeys, Temporal and spatial assessment of normal cerebrospinal fluid dynamics with MR imaging, Magn. Reson. Imaging 11 (8) (1993) 1107–1118, https://doi.org/10.1016/0730-725X(93)90238-9.